

PROCEEDINGS OF THE ROYAL SOCIETY A

MATHEMATICAL, PHYSICAL AND ENGINEERING SCIENCES

Modeling sediment compaction beneath ice lenses during frost heave

Journal:	<i>Proceedings A</i>
Manuscript ID	Draft
Article Type:	Research
Date Submitted by the Author:	n/a
Complete List of Authors:	Stubblefield, Aaron; Dartmouth College, Thayer School of Engineering Meyer, Colin; Dartmouth College, Thayer School of Engineering Rempel, Alan; University of Oregon, Department of Earth Sciences Warburton, Katarzyna; Dartmouth College, Thayer School of Engineering Hansen, Dougal; University of Wisconsin-Madison, Department of Geoscience Zoet, Lucas; University of Wisconsin-Madison, Department of Geoscience
Subject:	Glaciology < EARTH SCIENCES, Hydrology < EARTH SCIENCES, Mathematical modelling < MATHEMATICS
Keywords:	frost heave, frozen fringe, subglacial till, compaction modeling
Subject Category:	Earth Science

SCHOLARONE™
Manuscripts

Author-supplied statements

Relevant information will appear here if provided.

Ethics

Does your article include research that required ethical approval or permits?:

This article does not present research with ethical considerations

Statement (if applicable):

CUST_IF_YES_ETHICS :No data available.

Data

It is a condition of publication that data, code and materials supporting your paper are made publicly available. Does your paper present new data?:

Yes

Statement (if applicable):

The finite element code for solving the mathematical model and reproducing the figures is openly available (<https://github.com/agstub/compaction-frost>) and will be archived in a citeable form with Zenodo in the final version.

Conflict of interest

I/We declare we have no competing interests

Statement (if applicable):

CUST_STATE_CONFLICT :No data available.

PROCEEDINGS A

royalsocietypublishing.org/journal/rspa

Research



Article submitted to journal

Subject Areas:glaciology, mathematical modeling,
hydrology**Keywords:**frost heave, frozen fringe, subglacial
till, compaction modeling**Author for correspondence:**

A. G. Stubblefield

e-mail:

aaron.g.stubblefield@dartmouth.eduModeling sediment
compaction beneath ice
lenses during frost heaveA. G. Stubblefield¹, C. R. Meyer¹, A. W.
Rempel², K. L. P. Warburton¹, D. D.
Hansen³, and L. K. Zoet³¹Thayer School of Engineering, Dartmouth College,
Hanover, NH, USA²Department of Earth Sciences, University of Oregon,
Eugene, OR, USA³Department of Geoscience, University of
Wisconsin-Madison, Madison, WI, USA

Frost heave occurs when the ground swells during freezing conditions due to the growth of ice lenses in the subsurface. The mechanics of ice-infiltrated sediment, or frozen fringe, influences the formation and evolution of ice lenses. As the frozen fringe thickens during freezing, progressive unloading can result in dilation of the pore space and the formation of new ice lenses. Compaction can also occur as water is expelled from the pore space and freezes onto the ice lenses. We introduce a mathematical model for compaction within frozen fringe to explore how internal variability influences the fundamental characteristics of frost heave cycles. At faster freezing rates, compaction below ice lenses can generate complex dynamics and chaos when the frozen fringe follows a consolidation law based solely on the sediment yield stress. The complex oscillations arise because a downward water flux below the compacting zone generates a distributed zone of weakening. We introduce viscous effects into the compaction law through a bulk viscosity to determine how the cycles could be influenced by the creep of ice through the pore space. Localised zones of decompaction in the viscoplastic model can prevent the feedback mechanisms that cause complex oscillations in the perfectly plastic model.

© The Authors. Published by the Royal Society under the terms of the Creative Commons Attribution License <http://creativecommons.org/licenses/by/4.0/>, which permits unrestricted use, provided the original author and source are credited.

1. Introduction

Frost heave occurs when water is drawn out of the pore space in freezing soils to form layers of segregated ice in the subsurface, causing uplift of the overlying ground. Ice can infiltrate the pore space below ice lenses to form frozen fringes of sediment (figure 1) [1–6]. The presence of water below the bulk melting point in the frozen fringe is due to premelting, the formation of small amounts of water due to interfacial effects, the curvature of pore-throats, or the presence of impurities [7–9]. Premelting provides the thermomolecular forces that drive the segregation of ice and soil during frost heave [4,10].

As the frozen fringe grows during freezing, the load supported by contacts between sediment grains progressively reduces. New ice lenses are thought to form when the effective stress on the particle matrix vanishes and no forces restrain the ice from cleaving apart sediment grains [1,4]. Ice lenses can form repeatedly through this process during freezing conditions [11,12]. At slow freezing rates, ice lenses can instead grow steadily to form massive layers of ice, which have been found in exposed cliffs and sediment cores from permafrost regions [13–15].

Frozen fringes of sediment with interstitial ice and layers of debris-rich ice also exist in subglacial environments [14,16,17]. The growth of frozen fringe at the base of a glacier is a possible mechanism for the entrainment of sediment in glacial ice [18,19]. Entrained sediment influences the rheology of ice and the frictional behaviour between the basal ice and the underlying material [20–23]. Frozen fringes have been grown in the laboratory under subglacial conditions with a cryogenic ring shear device (figure 1) [24–26]. Recent experiments in the ring shear have shown that frozen fringe alters the frictional resistance between ice and the underlying sediment (figure 1b), which has been attributed to the formation of a softer mushy zone beneath a harder layer of fringe [26]. The evolution of subglacial frozen fringe therefore may influence the dynamics of ice streams and outlet glaciers that flow primarily through sliding over unconsolidated sediment [19,21]. The development of high-porosity shear bands during the growth of frozen fringe has also been observed in laboratory experiments (figure 1c) [24]. Similar shear bands have previously been found in experimental and theoretical studies of partially molten rocks and may contribute to the development of fluid-flow pathways [27–30].

Experimental studies of frost heave have generated periodic sequences of ice lenses by pulling water-saturated porous media through a fixed temperature gradient at a constant speed [31–35]. Previous theoretical work has focused on the idealised case of a constant porosity within the frozen fringe [4–6,36]. While a constant porosity within the fringe may be a reasonable approximation for overconsolidated soil, effective stress profiles from these studies suggest that sediment directly below the ice lens could potentially compact as water is drawn out of the fringe during freezing. Moreover, the water flux into the fringe caused by ice lens growth could potentially lead to dilation of the particle matrix. Laboratory experiments have shown that complex behaviour such as disordered or aperiodic ice segregation can arise from compaction [35]. Likewise, the frost heave model [4] was modified to include a parameterisation of an evolving compaction front below the fringe, which gave rise to complex behaviour that captured the essence of the laboratory experiments [36].

Modelling compaction in permeable media requires positing a relation between the porosity or material deformation and the effective stress, which is the difference between the stress on the solid matrix and the fluid pressure. Soil consolidation tests relate the effective yield stress of the sediment to the void ratio through empirical laws [37–39]. Empirical consolidation laws have not been experimentally validated in partially frozen sediments and, therefore, it remains uncertain whether or not they are appropriate for modelling compaction in frozen fringes. Moreover, mixtures of sediment and ice exhibit a bulk rheology where viscous effects arise above the sediment yield stress [20]. Alternatively, mixture theories developed for partially molten rocks assume that a viscous compaction law relates the divergence of the solid velocity to the pressure difference between the fluid and solid [27,28,40–42]. Constitutive relations that

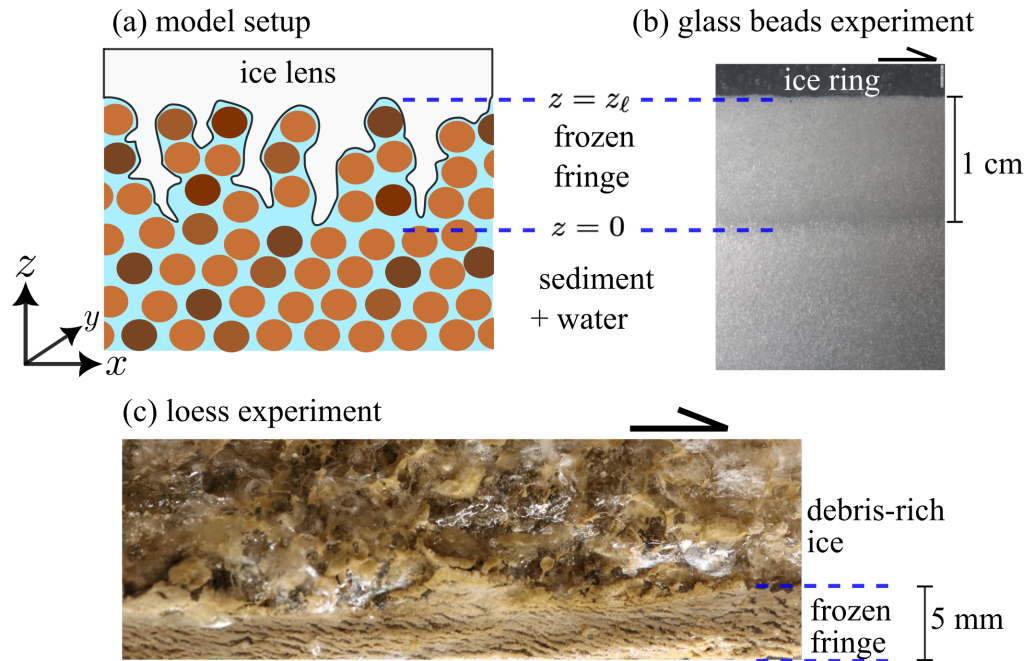


Figure 1. (a) Schematic of a frozen fringe of sediment below an ice lens [4]. The base of the ice lens is denoted by z_ℓ and the base of the frozen fringe is at $z = 0$. (b) Laboratory experiment in a cryogenic ring shear device showing growth of frozen fringe during shearing of the ice ring over a layer of water-saturated glass beads [26]. The sense of shear is shown by the arrow and the width of the frozen fringe is ~ 1 cm. Although not discernible in the photograph, a mushy layer of weakly frozen sediment formed near the base of the fringe [26]. (c) Ring shear experiment with Iowa loess showing the development of high-porosity shear bands below a layer of debris-rich ice [24]. The photo was taken after the ice ring was removed from the device and detached from the underlying unfrozen sediment. The width of the frozen fringe is ~ 5 mm.

incorporate both yielding and viscous effects have been used to model compaction and swelling in fibre suspensions [43,44].

Here, we develop a model for the compaction and dilation of frozen fringe during frost heave. We modify the mixture theory approach [40] to reproduce the key elements of frost heave models in the limit of a constant porosity [4]. While previous frost heave models rely on integral force balances [4,6], the mixture theory approach taken herein facilitates generalisations to higher spatial dimensions and alternative material behaviours. After deriving the model (section 2), we summarise the hierarchy of governing equations that arises from the different possible assumptions on the compaction law (section 3). We then describe how consolidation laws and bulk viscosity influence frost heave cycles relative to the constant porosity case (section 4). Finally, we conclude by discussing comparisons with previous work, possible generalisations of the theory, and avenues of future inquiry (section 5).

2. Model derivation

(a) Mass conservation

We consider a partially frozen mixture (frozen fringe) consisting of ice, water, and sediment beneath an ice lens (figure 1). We let ϕ denote the porosity, defined here as the volume fraction of the frozen fringe that is filled with water and ice. We define the ice saturation S as the fraction of pore space filled with ice. Ice lenses are characterised by regions where the ice completely saturates the pore space and sediment particles have been expelled so that $S = \phi = 1$. While

we restrict ourselves to the one spatial dimension in the vertical direction z , the mixture theory approach generalises to three spatial dimensions [40]. The base of the frozen fringe $z = 0$ is defined to be where the ice saturation vanishes ($S = 0$), marking the boundary between the frozen fringe and the underlying water-saturated sediment. We let $z = z_\ell$ denote the position of the ice lens, which is equivalent to the frozen fringe thickness in this coordinate system (figure 1).

We let v_i denote the ice velocity, v_s the sediment velocity, and v_w the water velocity. Conservation of mass for the ice, sediment, and water are given by

$$\frac{\partial}{\partial t} [\rho_i \phi S] + \frac{\partial}{\partial z} [\rho_i \phi S v_i] = \Gamma \quad (2.1)$$

$$\frac{\partial}{\partial t} [\rho_s (1 - \phi)] + \frac{\partial}{\partial z} [\rho_s (1 - \phi) v_s] = 0 \quad (2.2)$$

$$\frac{\partial}{\partial t} [\rho_w \phi (1 - S)] + \frac{\partial}{\partial z} [\rho_w \phi (1 - S) v_w] = -\Gamma, \quad (2.3)$$

respectively, where Γ is the freezing rate, ρ_i is the density of ice, ρ_s is the density of sediment, and ρ_w is the density of water. We will assume a constant ice velocity v_i for consistency with previous models of frost heave that assumed a rigid ice skeleton [4,6]; we show that deviations from a constant ice velocity are expected to be negligible for the parameters explored herein (see Appendix). The water flux relative to the sediment motion is defined by

$$q = \phi (1 - S) (v_w - v_s). \quad (2.4)$$

Mass balance for the total water content is obtained by summing (2.1) and (2.3) to obtain

$$\frac{\partial \phi}{\partial t} + \frac{\partial}{\partial z} [\phi S v_i + q + \phi (1 - S) v_s] = 0, \quad (2.5)$$

where we have made the approximation $(1/\rho_i) - (1/\rho_w) \approx 0$. The relative (scaled) density difference between ice and water, $(\rho_w - \rho_i)/\rho_w$, will be neglected herein although the relevant terms can be retained as shown in [6].

Jump conditions across the boundary between the ice lens and frozen fringe lead to a simplified relationship between the water flux and solid velocities. We assume that the ice saturation S and porosity ϕ jump to 1 at the ice lens $z = z_\ell$ and that the ice velocity v_i is continuous across this boundary. We integrate (2.2) and (2.5) across the jump at the ice lens to obtain

$$\dot{z}_\ell = v_s^- \quad (2.6)$$

$$q^- = (1 - \phi^- S^-) (v_i - v_s^-), \quad (2.7)$$

where $f^- = \lim_{z \rightarrow z_\ell^-} f(z)$. Using the definition of the water flux (2.4), we sum the mass balance equations (2.1)-(2.3) after dividing by the densities to obtain the constraint

$$\frac{\partial q}{\partial z} + \frac{\partial}{\partial z} [(1 - \phi S) v_s + \phi S v_i] = 0, \quad (2.8)$$

where we have again made the approximation $(1/\rho_i) - (1/\rho_w) \approx 0$. We integrate the flux constraint at the ice lens (2.8) and use (2.7) to find that

$$q = (1 - \phi S) v_*, \quad (2.9)$$

where we have defined the ice velocity relative to the sediment velocity to be

$$v_* = v_i - v_s, \quad (2.10)$$

which we will refer to as the heave rate [4].

To illuminate the roles of the heave rate and ice velocity, we rewrite the ice lens evolution equation (2.6) as

$$\dot{z}_\ell = v_i - v_*(z_\ell), \quad (2.11)$$

which shows that the heave rate at $z = z_\ell$ corresponds to the growth rate of the ice lens thickness when the upper surface of the ice lens moves at the ice velocity. Therefore, a positive heave rate at the ice lens causes the ground surface to swell over time due to the growth of segregated ice.

The lens evolution equation (2.11) also shows that the ice velocity v_i is analogous to the pulling speed in previous studies [4,35]. For this reason, we will often refer to the ice velocity as the pulling speed below. Assuming a constant ice velocity v_i , we rewrite the mass balance equation (2.2) in terms of the heave rate as

$$\frac{\partial \phi}{\partial t} + v_i \frac{\partial \phi}{\partial z} = - \frac{\partial}{\partial z} [(1 - \phi)v_*], \quad (2.12)$$

which shows that the ice velocity v_i is associated with advection of the sediment.

The primary mass-balance equations that we use in the remainder of the derivation are the water flux (2.9), the ice-lens evolution (2.11), and the porosity evolution (2.12), which are all written in terms of the heave rate v_* . Therefore, before continuing with the momentum balance, we first describe the relationships between the heave rate, freezing rate, and ice velocity. We integrate (2.1) and use (2.11) to obtain the ratio

$$\frac{v_*(z_\ell)}{v_i} = \frac{\int_0^{z_\ell} \Gamma dz - \frac{d}{dt} \left[\int_0^{z_\ell} \rho_i \phi S dz \right]}{[\rho_i \phi S v_i]_{z=z_\ell}}. \quad (2.13)$$

The ratio (2.13) shows that the heave rate is positive when the net freezing rate exceeds the rate of ice mass change within the fringe, which results in growth of the ice lens. On the other hand, equations (2.11) and (2.13) imply that the frozen fringe grows ($\dot{z}_\ell > 0$) whenever the rate of ice mass change within the fringe exceeds the difference between the net freezing rate and the ice flux into the lens. In the limit of a constant porosity and time-independent ice saturation, equation (2.1) shows that the ice velocity (pulling speed) equals the net freezing rate relative to the ice mass directly below the lens.

(b) Momentum conservation

In deriving the momentum balance, we follow previous formulations for partially molten mixtures [40,41]. We show below that this formulation is consistent with previous frost heave models that have been formulated with integral force balances in the vertical direction [6,18]. We denote the water pressure by p_w and the normal stress in the vertical direction on the ice and sediment phases by σ_i and σ_s , respectively. Momentum balance for the partially frozen mixture is given by

$$\frac{\partial}{\partial z} [-\phi S \sigma_i] + F_i = \phi S \rho_i g \quad (2.14)$$

$$\frac{\partial}{\partial z} [-(1 - \phi) \sigma_s] + F_s = (1 - \phi) \rho_s g \quad (2.15)$$

$$\frac{\partial}{\partial z} [-\phi(1 - S) p_w] + F_w = \phi(1 - S) \rho_w g, \quad (2.16)$$

where F_i , F_s , and F_w are interfacial forces on the ice, sediment, and water, respectively [40,45]. While we assume that the ice skeleton is rigid ($\sigma_i = p_i$) for the parameters explored herein, the derivation generalises to the case of deforming ice (Appendix).

We set the interfacial force on the water F_w to be

$$F_w = -d(v_w - v_s) + p_w \frac{\partial}{\partial z} [\phi(1 - S)] \quad (2.17)$$

$$d = \frac{\mu[\phi(1 - S)]^2}{k}, \quad (2.18)$$

which, along with (2.16), results in Darcy's law

$$q = -\frac{k}{\mu} \left(\frac{\partial p_w}{\partial z} + \rho_w g \right), \quad (2.19)$$

where k is the permeability, μ is the viscosity of water, and g is gravitational acceleration.

We choose the interfacial force on the ice and sediment to be

$$F_i = p_w \frac{\partial}{\partial z} [\phi S] + (p_i - p_w) \frac{\partial}{\partial z} [\phi S] \quad (2.20)$$

$$F_s = d(v_w - v_s) + p_w \frac{\partial}{\partial z} [1 - \phi] + (p_i - p_w) \frac{\partial}{\partial z} [1 - \phi S], \quad (2.21)$$

so that all of the interfacial forces balance. The interfacial forces (2.20)-(2.21) mirror the magma dynamics formulation [40], with the addition of terms proportional to the pressure difference between ice and water ($p_i - p_w$) that represent thermomolecular forces related to premelting at the ice-water interface [4]. In particular, the interfacial force (2.20) can be written as $F_i = p_i \frac{\partial}{\partial z} [\phi S]$, which represents the ice pressure acting normal to the unfrozen material interface. Equation (2.14) implies that the interfacial force F_i results in a cryostatic ice pressure gradient in the rigid ice limit ($\sigma_i = p_i$), which is consistent with the conceptual model of a rigid ice skeleton (figure 1).

We sum the momentum balance equations for the unfrozen component (2.15)-(2.16) and use $F_s + F_w = -F_i$ to obtain the force balance

$$\frac{\partial}{\partial z} [(1 - \phi)\sigma_s - \phi(1 - S)p_w] + p_i \frac{\partial}{\partial z} [1 - \phi S] = \rho_s g(1 - \phi) + \rho_w g\phi(1 - S). \quad (2.22)$$

We define the effective stress on the sediment particles to be

$$N = (1 - \phi)(\sigma_s - p_w), \quad (2.23)$$

which will be related to porosity through a compaction law below (section 2(c)). Using the definition (2.23), the bulk momentum equation (2.22) becomes

$$\frac{\partial N}{\partial z} = -\frac{\partial}{\partial z} [(1 - \phi S)p_w] + p_i \frac{\partial}{\partial z} [1 - \phi S] - \rho_s g(1 - \phi) - \rho_w g\phi(1 - S). \quad (2.24)$$

We derive a boundary condition for the effective stress below the ice lens from a jump condition across the interface. The ice momentum balance (2.14) implies

$$p_i \frac{\partial}{\partial z} [1 - \phi S] = -\frac{\partial}{\partial z} [\phi S p_i] - \phi S \rho_i g. \quad (2.25)$$

Noting that the effective stress (2.23) jumps to zero at the ice lens, we integrate equation (2.24) across the jump and use (2.25) to obtain

$$N^- = (1 - \phi^- S^-)(p_i^- - p_w^-). \quad (2.26)$$

Equation (2.26) represents the thermomolecular force acting on the unfrozen material below the ice lens.

We isolate the thermomolecular effects by rewriting the momentum balance (2.24) as

$$\frac{\partial N}{\partial z} = -(1 - \phi S) \frac{\partial p_w}{\partial z} - (p_i - p_w) \frac{\partial}{\partial z} [\phi S] - \rho_s g(1 - \phi) - \rho_w g\phi(1 - S), \quad (2.27)$$

which is consistent with the integral force balance in previous models [6]. We determine the thermomolecular term by using the generalized Clausius-Clapeyron equation,

$$p_i - p_w = \rho_i \mathcal{L} \frac{T_m - T}{T_m} + (p_m - p_w) \frac{\rho_w - \rho_i}{\rho_w}, \quad (2.28)$$

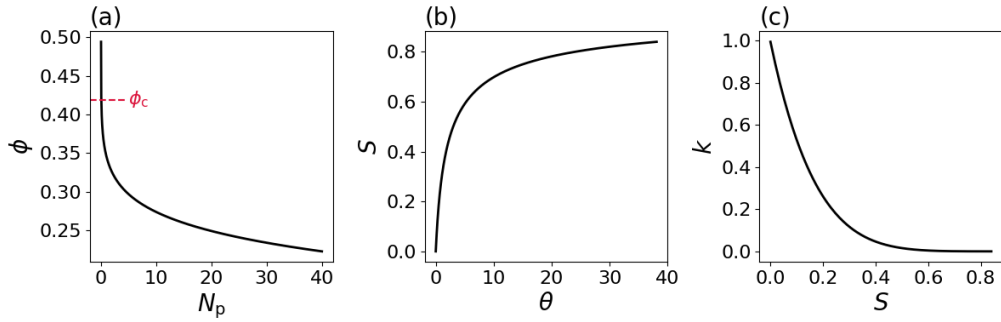


Figure 2. Nondimensional empirical relations, which depend on the parameters listed in table 1. (a) Porosity ϕ as a function of the yield stress N_p from the consolidation law (2.41). The porosity $\phi_c = 0.42$ denotes the threshold where lens nucleation occurs according to (3.14) in the perfectly plastic compaction model. The corresponding effective stress threshold is $N_c = 0.05$, or a dimensional stress of 3.4 kPa according to the scale in table 1. (b) Ice saturation S (2.46) as a function of undercooling temperature θ . (c) Relative permeability k (2.47) as a function of the ice saturation S .

where T is the temperature, \mathcal{L} is the latent heat, and (T_m, p_m) are a reference temperature and pressure [46,47]. To determine the temperature T , we will adopt a frozen-temperature approximation for simplicity below (section 2(e)). The term involving the relative density difference between ice and water in (2.28) is small and will be neglected [6].

We combine the water flux expression (2.9) and Darcy's law (2.19) to obtain the identity

$$\frac{\partial p_w}{\partial z} = - \left[\rho_w g + \frac{\mu}{k} (1 - \phi S) v_* \right]. \quad (2.29)$$

Using (2.28) and (2.29) in the momentum balance (2.27), we obtain

$$\frac{\partial N}{\partial z} = \frac{\mu}{k} (1 - \phi S)^2 v_* - \left(\rho_i \mathcal{L} \frac{T_m - T}{T_m} \right) \frac{\partial}{\partial z} [\phi S] - (\rho_s - \rho_w) g (1 - \phi). \quad (2.30)$$

Similarly, the expression (2.26) for the effective stress below the ice lens becomes

$$N^- = (1 - \phi^- S^-) \left(\rho_i \mathcal{L} \frac{T_m - T^-}{T_m} \right). \quad (2.31)$$

(c) Compaction laws

We consider compaction laws of the form

$$N = N_p(\phi) + N_* \quad (2.32)$$

where N_p is a plastic yield stress that depends only on the porosity and N_* is an additional stress that allows for unloading ($N \rightarrow 0$). We explain why the additional term N_* is necessary for unloading and consider two different options below.

Soil consolidation tests relate the void ratio $e = \phi/(1 - \phi)$ to the effective stress through empirical relations of the form

$$e(N_p) = e_0 - b \log(N_p/N_0), \quad (2.33)$$

where e_0 is the void ratio at a reference load of $N_0 = 1$ kPa and b is an empirical constant [38]. We choose typical parameter values for normal consolidation of subglacial till with $e_0 = 0.8$ and $b = 0.15$ (table 1). Other empirical relations between porosity and effective stress that hold for overconsolidation (unloading-reloading line) or shearing (critical state line) can be incorporated in this framework [37,39]. The empirical relation for porosity is obtained from (2.33) via $\phi(N_p) = e(N_p)/[1 + e(N_p)]$. While the porosity approaches unity in the limit $N_p \rightarrow 0$, this is associated with a singularity in the gradient of the consolidation law, $|\phi'(N_p)| \rightarrow \infty$ (figure 2). Thus, small

changes in the effective stress result in large changes in the porosity in the limit $N_p \rightarrow 0$, which influences the nucleation of ice lenses.

Previous models of frost heave with constant porosity assume that new ice lenses nucleate when the total effective stress reaches zero, $N \rightarrow 0$, within the fringe [1,4,6]. When the effective stress reaches zero, no forces restrain ice from cleaving apart the particle matrix and a new ice lens forms. We demonstrate below (section 3(e)) that the plastic yield stress N_p cannot vanish due to the presence of the gradient singularity in the empirical law (2.41). Therefore, we must consider other mechanisms that allow for unloading. For example, we could assume that a tensile stress $N_* = -N_c$ is generated by small, ice-filled cracks in accordance with previous work [48,49]. In this case, the total effective stress will vanish once a threshold porosity $\phi_c = \phi(N_c) < 1$ is reached (figure 2). We assume that crack propagation causes the nucleation of a new ice lens in this case. For simplicity, we will consider a constant value of $N_c = 3.4$ kPa, which is a small fraction of the effective stress scale described below (table 1). For example, this threshold would correspond to a flaw of size ~ 5 cm when the fracture toughness is 10^3 Pa m^{1/2} (e.g., Kaolinite clay) or ~ 0.5 mm when the fracture toughness is 10^2 Pa m^{1/2} (e.g., silica microspheres) [48].

An alternative mechanism to cracking is viscous infiltration, which is motivated by the consideration of ice leaving the pore space upon consolidation or entering the pore space upon dilation. The movement of ice through pores imposes a time scale in response to stress variations that is not captured by the plastic consolidation law (2.33). Because ice deforms viscously over long time scales [50,51], we generalise the stress N_* to include a viscous term,

$$N_* = -N_c + (1 - \phi)\zeta \frac{\partial v_*}{\partial z}, \quad (2.34)$$

where ζ is the bulk viscosity of the mixture [40]. While ζ could depend on the porosity or ice saturation, we will assume that it is constant for simplicity. The effective stress (2.32) with the viscous contribution (2.34) mirrors a debris-rich ice rheology where viscous deformation occurs above the sediment yield stress [20]. While the ice is approximated as rigid in our formulation (Appendix), we assume that the bulk mixture deforms viscously because the presence of ice in the pore space potentially limits the rate of sediment consolidation. The combination of viscous compaction and plastic consolidation appears in other applications where there is both yielding and rate-dependent behaviour such as in the compaction or swelling of fibre (e.g., cellulose) suspensions [43,44]. We show below that including either the constant tensile stress or viscous stress in the compaction law (2.32) allows for the generation of ice lenses ($N \rightarrow 0$).

(d) Scaling

We scale the effective stress by the threshold $[N]$ needed for ice to overcome the curvature of the pore throats and infiltrate the sediment. This threshold is determined by the Gibbs-Thomson effect to be

$$[N] = \frac{2\gamma_{iw}}{r_p}, \quad (2.35)$$

where γ_{iw} is the interfacial energy and r_p is the pore-throat radius [6,18]. Owing to the Clausius-Clapeyron relation (2.28), the temperature T_f where ice begins to infiltrate is

$$T_f = T_m \left(1 - \frac{[N]}{\rho_i \mathcal{L}} \right), \quad (2.36)$$

which is the temperature at the base of the fringe ($z = 0$). With the values in table 1, ice infiltrates at $T_f = 273.09$ K. With these considerations, we scale the variables according to

$$[z] = \frac{[N]}{(\rho_s - \rho_w)g}, \quad [v] = \frac{[k](\rho_s - \rho_w)g}{\mu}, \quad [t] = \frac{[z]}{[v]}, \quad [T] = \frac{T_m [N]}{\rho_i \mathcal{L}}. \quad (2.37)$$

We scale both the ice velocity v_i and heave rate v_* by the same velocity scale $[v]$, which depends on the permeability scale $[k]$ that is described below (section 2(e)).

Physical parameters		Scales	Nondimensional parameters		
ρ_i	917 kg m^{-3}	$[N]$	68 kPa	α	6
ρ_w	1000 kg m^{-3}	$[z]$	4.62 m	β	0.5
ρ_s	2500 kg m^{-3}	$[v]$	15.5 m yr^{-1}	a	68
g	9.81 m s^{-2}	$[t]$	0.3 yr	b	0.15
\mathcal{L}	$3.34 \times 10^5 \text{ J kg}^{-1}$	$[k]$	$6 \times 10^{-14} \text{ m}^2$	c	1.9
γ_{iw}	0.034 J m^{-2}	$[T]$	0.06 K	e_0	0.8
μ	$1.8 \times 10^{-3} \text{ Pa s}$	–	–	λ	$[0, 4]$
r_p	10^{-6} m	–	–	N_c	$[0, 0.5]$
T_m	273.15 K	–	–	N_f	$[1.6, 2]$
ζ	$[0, 10^{13}] \text{ Pa s}$	–	–	v_i	$[0.012, 0.074]$
δ	$[0, 18.5] \text{ m}$	–	–	–	–

Table 1. Values for physical parameters, scales, and nondimensional parameters. Ranges are provided for the parameters that are varied between numerical experiments.

We shift the temperature to coincide with zero at the base of the fringe by defining the (scaled) undercooling temperature

$$\theta = \frac{T_f - T}{[T]}. \quad (2.38)$$

Without renaming the other nondimensional variables, the momentum balance (2.30) scales to

$$\frac{\partial N}{\partial z} = \frac{1}{k}(1 - \phi S)^2 v_* - (1 + \theta) \frac{\partial}{\partial z}[\phi S] - (1 - \phi). \quad (2.39)$$

The porosity evolution equation (2.12) and lens evolution equation (2.11) take the same forms under this scaling, while the effective stress beneath the ice lens (2.31) becomes

$$N^- = (1 - \phi^- S^-)(1 + \theta^-). \quad (2.40)$$

We scale both the yield stress and the viscous stress in the compaction law (2.32) by $[N]$. Likewise, the empirical consolidation law (2.33) scales to

$$e(N_p) = e_0 - b \log(a N_p) \quad (2.41)$$

where $a = [N]/N_0$. The viscous stress (2.34) scales to

$$N_* = -N_c + \lambda^2 (1 - \phi) \frac{\partial v_*}{\partial z} \quad (2.42)$$

where we have defined the parameter

$$\lambda = \frac{\delta}{[z]}. \quad (2.43)$$

The parameter λ relates the length scale set by infiltration $[z]$ to the classical viscous compaction length δ , which is here defined by

$$\delta = \sqrt{\frac{[k]}{\mu}} \zeta. \quad (2.44)$$

In our formulation, the compacting phase (soil) is not viscous whereas in the magma dynamics formulation [40] an additional term involving the viscosity of the compacting phase appears in the length scale δ (2.44). Example parameter values are provided in table 1.

(e) Constitutive relations

We require constitutive relations for the permeability and ice saturation, which depend on the undercooling temperature θ . For comparison with previous studies, we assume a frozen-temperature approximation with constant gradient,

$$\theta = cz, \quad (2.45)$$

where $c = |\frac{dT}{dz}|[z]/[T]$ is the nondimensional temperature gradient [4,36]. We set $c = 1.9$, which corresponds to a temperature gradient of 25 K/km with the scales in table 1. This geothermal temperature gradient is motivated by conductive cooling, for example, beneath a glacier of thickness 1 km with a surface temperature near -25°C . Higher temperature gradients that are appropriate for (subaerial) permafrost and laboratory experiments are considered in the discussion. This simplification allows us to focus on the mechanical effects of compaction on the frost heave cycles. Models that instead solve the full energy balance to determine the temperature evolution have also been developed [5,6].

Empirical relations for the saturation and permeability are given by

$$S(\theta) = \max(0, 1 - |1 + \theta|^{-\beta}) \quad (2.46)$$

$$k(S) = (1 - S)^\alpha, \quad (2.47)$$

where the permeability law has been scaled by $[k]$ (table 1). The permeability scale $[k]$ can vary over several orders of magnitude and, therefore, strongly influences the time scale $[t]$ (2.37) [52,53]. We choose typical values for the exponents $\alpha = 6$ and $\beta = 0.5$ [18]. The empirical laws (2.46)-(2.47) imply that the permeability decreases as the ice saturation increases and that the pore space becomes increasingly saturated with ice at larger undercooling temperatures (figure 2). In particular, the permeability decreases and the ice saturation increases beneath the ice lens as the fringe grows under a constant temperature gradient.

3. Governing equations

Now we state the final governing equations and then consider the simplified cases of perfectly plastic compaction ($\lambda = 0$) and constant porosity. We then discuss the boundary conditions and the ice lens nucleation conditions. The full model involves solving for the heave rate to evolve the fringe thickness ($\dot{z}_\ell = v_i - v_*$) and the effective stress to evaluate the nucleation condition ($N = 0$). We discuss below how the degree of coupling between these steps depends on the choice of compaction law.

(a) Viscoplastic compaction

We combine the mass and momentum balances to derive a coupled set of partial differential equations for the yield stress and the heave rate. The heave rate is determined from equation (2.39) to be

$$v_* = \frac{k}{(1 - \phi S)^2} \left[\frac{\partial N}{\partial z} + (1 + \theta) \frac{\partial}{\partial z} [\phi S] + 1 - \phi \right]. \quad (3.1)$$

Substituting the heave rate (3.1) and compaction law $N = N_p + N_*$, with N_* determined by (2.42), into the mass balance equation (2.12), we obtain

$$\frac{\partial}{\partial t} [1 - \phi] + v_i \frac{\partial}{\partial z} [1 - \phi] = \frac{\partial}{\partial z} \left[D(\phi, S) \frac{\partial N_p}{\partial z} \right] + F(\phi, S) + H(v_*), \quad (3.2)$$

where we have defined the effective diffusivity and forcing functions

$$D(\phi, S) = \frac{(1 - \phi)}{(1 - \phi S)^2} k \quad (3.3)$$

$$F(\phi, S) = \frac{\partial}{\partial z} \left[D(\phi, S) \left((1 + \theta) \frac{\partial}{\partial z} [\phi S] + 1 - \phi \right) \right] \quad (3.4)$$

$$H(v_*) = \frac{\partial}{\partial z} \left[D(\phi, S) \frac{\partial}{\partial z} \left[\lambda^2 (1 - \phi) \frac{\partial v_*}{\partial z} \right] \right]. \quad (3.5)$$

For a general constitutive relation $\phi = \phi(N_p)$, equation (3.2) can be written as a nonlinear advection-diffusion equation for the yield stress,

$$|\phi'(N_p)| \left(\frac{\partial N_p}{\partial t} + v_i \frac{\partial N_p}{\partial z} \right) = \frac{\partial}{\partial z} \left[D(\phi, S) \frac{\partial N_p}{\partial z} \right] + F(\phi, S) + H(v_*), \quad (3.6)$$

where coupling with the heave rate occurs through the forcing function H . When viscous effects are included ($\lambda > 0$), equation (3.6) is coupled to an elliptic equation for the heave rate that follows from rearranging (3.1),

$$-\frac{\partial}{\partial z} \left[\lambda^2 (1 - \phi) \frac{\partial v_*}{\partial z} \right] + \frac{(1 - \phi S)^2}{k} v_* = \frac{\partial N_p}{\partial z} + (1 + \theta) \frac{\partial}{\partial z} [\phi S] + 1 - \phi. \quad (3.7)$$

The full viscoplastic compaction problem is to solve the coupled equations (3.6)-(3.7) for (N_p, v_*) subject to the boundary conditions on the yield stress and heave rate discussed below (section 3(d)). In this way, there is a two-way coupling between the effective stress and the heave rate in the full viscoplastic model. In the following sections, we simplify the full governing equations (3.6)-(3.7) by considering the limits of perfectly plastic compaction ($\lambda = 0$) and constant porosity ($\phi'(N_p) = 0$).

(b) Perfectly plastic compaction

We consider the simplified case where viscous effects are neglected in the full problem (3.6)-(3.7), which corresponds to the limit $\lambda \rightarrow 0$ where the effective stress simplifies to $N \equiv N_p(\phi) - N_c$. In this limit, the heave-rate forcing term H (3.5) vanishes so that we only need to solve the advection-diffusion equation (3.6) for the yield stress. The heave rate can then be calculated directly from (3.7) upon setting $\lambda = 0$. Therefore, there is a one-way coupling between the effective stress and heave rate when viscous effects are neglected. The limit $\lambda \rightarrow 0$ represents a singular perturbation of the full model (3.7). We describe how the boundary conditions change in this limit relative to the full problem below (section 3(d)).

The assumption of perfectly plastic compaction has consequences for ice lens nucleation when a logarithmic consolidation law is adopted. The gradient singularity in the consolidation law, $|\phi'(N_p)| \rightarrow \infty$ as $N_p \rightarrow 0$ (figure 2a), results in pure advection in equation (3.6). While the limit of pure advection is consistent with the conceptual model of a rigid ice lens forming as $\phi \rightarrow 1$, the singularity prevents $N = 0$ from being attained exactly unless there is a preexisting tensile stress $N_c > 0$ as discussed previously (section 2(c)).

(c) Constant porosity

As a final simplification, we also consider the case of a constant porosity for comparison with previous theoretical studies that adopted this assumption [4–6,36]. In the context of our model, the constant porosity assumption can be viewed as an approximation for overconsolidated soil where the void ratio is insensitive to changes in stress from unloading or reloading ($\phi'(N_p) \approx 0$). The tensile stress N_c is not necessary for unloading to occur in the constant porosity model. Moreover, equation (2.12) implies that the heave rate is spatially uniform when the porosity is constant. Therefore, we set $N \equiv N_p$, neglecting viscous stresses and the preexisting tensile stress. In this limit, we obtain an ordinary differential equation for the lens evolution, $\dot{z}_\ell = v_i - v_*(z_\ell)$.

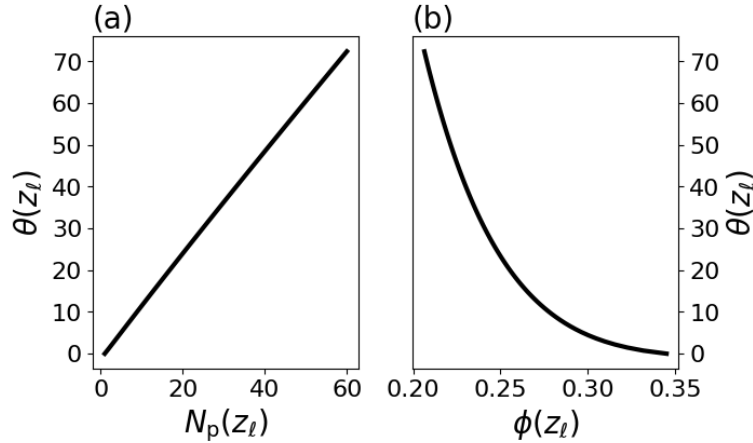


Figure 3. (a) Effective stress below the ice lens as a function of the undercooling at the ice lens $\theta(z_\ell)$. The effective stress is calculated from equations (2.41) and (3.11) with a root-finding algorithm. (b) Porosity below the ice lens corresponding to the effective stress in (a). Compaction below the ice lens increases with the undercooling $\theta(z_\ell)$. For reference, an undercooling of $\theta = 70$ corresponds to a dimensional temperature change of $T_f - T \approx 4.2$ K with the scale in table 1.

The effective stress below the ice lens $N_p = (1 - \phi S)(1 + \theta)$, i.e. (2.40), can be expressed as

$$N_p(z_\ell) = 1 + \int_0^{z_\ell} \frac{\partial}{\partial z} [(1 - \phi S)(1 + \theta)] dz \quad (3.8)$$

because $(1 - \phi S)(1 + \theta) = 1$ at the base of the fringe. Setting $\lambda = 0$, we integrate (3.7) and use (3.8) to obtain an expression for the heave rate,

$$v_*(z_\ell) = \frac{1 - N_f + \int_0^{z_\ell} 1 - \phi + (1 - \phi S) \frac{\partial \theta}{\partial z} dz}{\int_0^{z_\ell} \frac{1}{k} (1 - \phi S)^2 dz}, \quad (3.9)$$

where $N_f = N_p(0)$ is a prescribed effective stress at the base of the fringe. The boundary condition N_f is the load borne by particle contacts at the uppermost extent of water-saturated sediments and as such can be identified with the basal effective stress in studies of glacier mechanics [54,55]. The heave rate (3.9) is consistent with previous models that assumed a constant porosity [4,6,18,36].

To evaluate the lens initiation conditions ($N = 0$) as described below (section 3(e)), we integrate the force balance (2.39) to obtain the effective stress profile at z for a given lens position z_ℓ ,

$$N_p(z) = N_f + \int_0^z \left[\frac{1}{k} (1 - \phi S)^2 v_*(z_\ell) - \phi(1 + \theta) \frac{\partial S}{\partial z'} - (1 - \phi) \right] dz'. \quad (3.10)$$

Thus, the heave rate and lens initiation condition can be determined as functions of the porosity ϕ , fringe thickness z_ℓ , and basal effective stress N_f from equations (3.9) and (3.10) *a priori* in the constant porosity model. In contrast to the compaction models, the heave rate (3.9) and stress profile (3.10) do not directly depend on the pulling speed v_i .

(d) Boundary conditions

In the advection-diffusion equation (3.6), we prescribe Dirichlet conditions on the yield stress N_p so that the model reduces to the constant porosity model (section 3(c)) in the absence of porosity variations. We ascribe the effective stress condition below the ice lens (2.40) to the yield stress at

$$z = z_\ell,$$

$$N_p(z_\ell) = (1 - \phi S)(1 + \theta). \quad (3.11)$$

The boundary condition (3.11) implies that compaction occurs below the ice lens as the undercooling increases. In a fixed temperature gradient, the porosity below the ice lens becomes a function of the fringe thickness (or undercooling) alone due to this boundary condition and can be obtained numerically with a root-finding method (figure 3). At the base of the fringe ($z = 0$), we prescribe a constant effective stress

$$N_p(0) = N_f, \quad (3.12)$$

following previous studies [6,18]. The boundary condition (3.12) results in a fixed porosity at the base of the fringe, $\phi_f = \phi(N_f)$.

When viscous effects are included ($\lambda > 0$) in the compaction relation (2.42), we must also supply boundary conditions on the elliptic equation for the heave rate (3.7). As we have ascribed the stress conditions to the yield stress, we assume that the viscous stresses vanish at the boundaries,

$$\frac{\partial v_*}{\partial z} = 0 \quad (3.13)$$

below the ice lens ($z = z_\ell$) and at the base of the fringe ($z = 0$). This choice is consistent with the constant porosity model where v_* is spatially uniform, as well as the requirement that the viscous stresses should vanish below the fringe in the ice-free sediment. However, it is possible that a portion of the total effective stress below the lens, $N(z_\ell) = (1 - \phi S)(1 + \theta)$, could be ascribed to viscous stresses, although we cannot currently constrain such a partitioning. The perfectly plastic limit $\lambda \rightarrow 0$ (section 3(b)) represents a singular perturbation of the elliptic equation (3.7) where gradients in the heave rate at the boundaries are determined by the yield stress alone.

(e) Ice lens nucleation

We assume that a new ice lens will initiate at a position z_n and a discrete point in time t_n when the total effective stress $N = N_p + N_*$ reaches zero [1,4]. Thus, the position of the active ice lens jumps in time,

$$\begin{cases} N(z_n, t_n^-) = 0 \\ z_\ell(t_n^+) = z_n \end{cases}, \quad (3.14)$$

where t_n^- and t_n^+ denote before and after the jump, respectively. Likewise, we define the maximum lens position via $z_\ell(t_n^-) = z_m$. We refer to z_m as the maximum fringe thickness and z_n as the incipient fringe thickness. The jumps in frozen fringe thickness ($z_m - z_n$) correspond to the spacing between successive ice lenses.

Immediately after an ice lens nucleates, we must specify a stress field on the new domain $[0, z_n]$ that satisfies the boundary conditions (3.11)-(3.13). Here, we assume that the sediment is advecting with the pulling speed (ice velocity) immediately after nucleation. In the discussion, we describe how dynamic cracking models and experiments could further constrain the behaviour of frozen fringe during lens nucleation (section 5). Therefore, we neglect the material derivative in (3.6) so that the yield stress immediately after lens nucleation is determined by the elliptic equation

$$-\frac{\partial}{\partial z} \left[D(\phi, S) \frac{\partial N_p}{\partial z} \right] = F(\phi, S) + H(v_*) \quad (t = t_n^+), \quad (3.15)$$

which is coupled to the elliptic equation for the heave rate (3.7) when $\lambda > 0$. Thus, the stress profile immediately after lens initiation only depends on the new lens position z_n , which is consistent with the constant porosity model (3.10). By adopting the nucleation conditions (3.14)-(3.15), we only resolve the dynamics below the new (active) ice lens at any point in time. We assume that

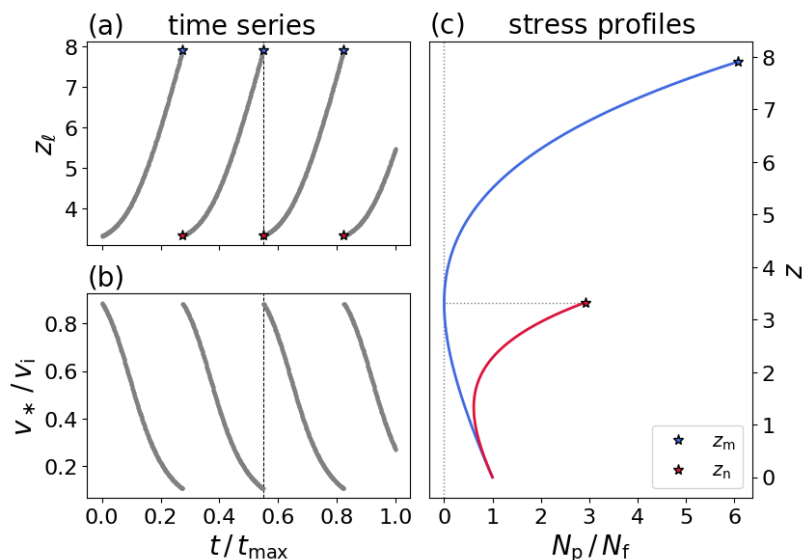


Figure 4. Evolution of the (a) ice lens position and (b) heave rate for the constant porosity model with the pulling speed $v_i = 0.03$ and effective stress at the base of the fringe $N_f = 2$. The maximum time is $t_{\max} = 1000$. (a) Ice lenses are periodically generated for these values of the pulling speed and effective stress. The maximum fringe thicknesses are denoted by blue stars and the incipient fringe thicknesses are denoted by red stars. (b) The heave rate is monotonically decreasing over time. (c) Stress profiles at the maximum fringe thickness z_m (blue) and incipient fringe thickness z_n (red) at the time noted by the vertical dashed line in the time series. The ice lens nucleates at z_n because $N(z_n) = 0$ when the fringe thickness reaches its maximum. During the next cycle, the fringe starts at the incipient thickness z_n .

the old ice lens stops growing because the water supply from below the fringe has been cut off by a new impermeable layer of ice.

4. Results

We solve the governing equations (3.6)-(3.7) subject to the boundary conditions (3.11)-(3.13), nucleation conditions (3.14)-(3.15), and lens evolution equation (2.11) with the finite element package FEniCS [56–58]. The code for solving the problem and reproducing the figures is openly available (<https://github.com/agstubb/comaction-frost>) and will be archived in a citeable form with Zenodo in the final version.

The primary parameters in the scaled problem are the ice velocity v_i , the effective stress boundary condition at the base of the fringe N_f , and the bulk viscosity parameter λ . We first consider the case of constant porosity as a reference solution (section 4(a)). We then explore how perfectly plastic compaction ($\lambda = 0$) can generate complex oscillations in the frost heave cycles that depend on v_i and N_f (section 4(b)). Finally, we explore how viscous effects ($\lambda > 0$) can inhibit the feedbacks that lead to complex oscillations in the perfectly plastic model (section 4(c)).

(a) Constant porosity

As a reference solution for the compaction problems, we first consider the constant porosity problem as described in section 3(c) and in previous work [4]. In the constant porosity limit, equation (2.1) shows that the ice velocity v_i (pulling speed) is proportional to the net freezing rate. To facilitate comparisons between the models, we set the pulling speed to $v_i = 0.03$ and the stress boundary condition to $N_f = 2$ because ice lenses are generated repeatedly for these parameter values in all of the models (e.g., figure 4a). The constant porosity model predicts that the heave

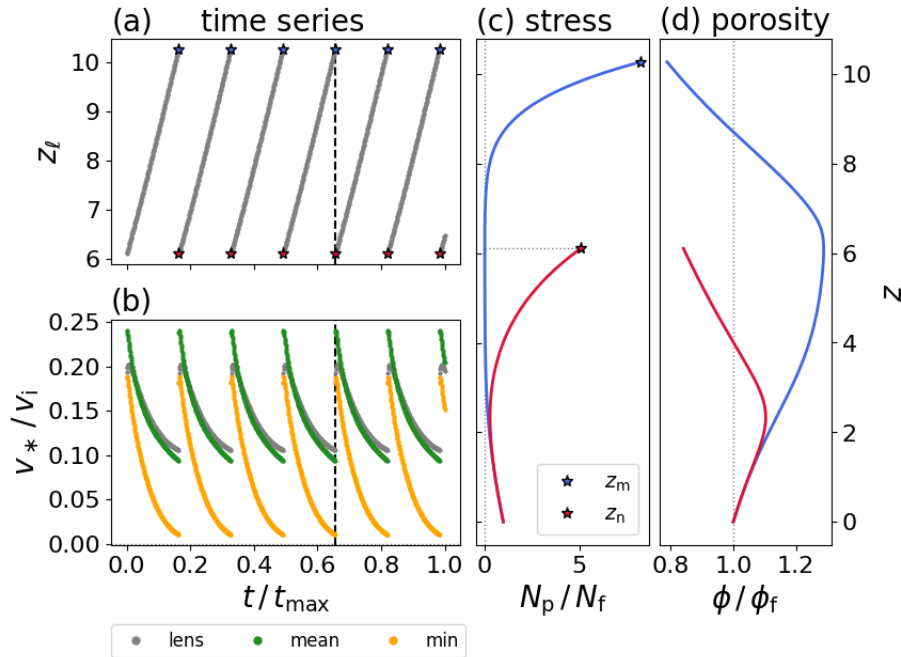


Figure 5. Evolution of the (a) ice lens position and (b) heave rate for the perfectly plastic compaction model ($\lambda = 0$) with the same parameters as in figure 4. The pulling speed is $v_i = 0.03$ and the effective stress at the base of the fringe is set to $N_f = 2$, which corresponds to a porosity of $\phi_f = 0.325$. The maximum time is $t_{max} = 1000$. (a) Ice lenses are periodically generated for these parameter values. (b) The heave rate decreases over time throughout the fringe for these parameters. (c) Stress profiles at the maximum fringe thickness (blue) and incipient fringe thickness (red) at the time noted by the dashed vertical line in the time series. (d) Porosity profiles at the maximum and incipient fringe thicknesses. Dilation ($\phi > \phi_f$) occurs throughout most of the fringe while compaction ($\phi < \phi_f$) occurs below the ice lens.

rate decreases over time (figure 4b). As the frozen fringe thickens over time, the ice lens growth slows because the permeability decreases as the ice saturation increases at higher undercooling temperatures below the lens (figure 2). Thus, the rate of water supply to the growing ice lens diminishes over time in accordance with the relation (2.9). The frozen fringe eventually reaches a maximum thickness z_m and a new ice lens nucleates at z_n (figure 4c).

When the incipient fringe thickness z_n is large enough, the fringe will continue to grow again in the next cycle and the process will repeat. Otherwise, the frozen fringe will approach a steady state ($v_* = v_i$) where a single ice lens grows steadily. The onset of oscillations and the stability of steady solutions in the constant porosity problem have been described previously [4–6]. Here, we instead focus on the qualitative behaviour of the frost heave cycles rather than the conditions that produce the oscillations. In the following sections, we explore how internal variability driven by compaction below the ice lens can lead to more complex dynamics.

(b) Plastic model

Now, we explore the behaviour of the perfectly plastic model by solving (3.6)-(3.7) with $\lambda = 0$ as described in section 3(b). We set the tensile stress that allows for lens nucleation by crack propagation to $N_c = 0.05$, which corresponds to a porosity threshold of $\phi_c = 0.42$ (figure 2a). We first examine the model behaviour for different values of the pulling speed v_i at a fixed value of effective stress boundary condition, $N_f = 2$. We will then explore the effect of varying the stress boundary condition.

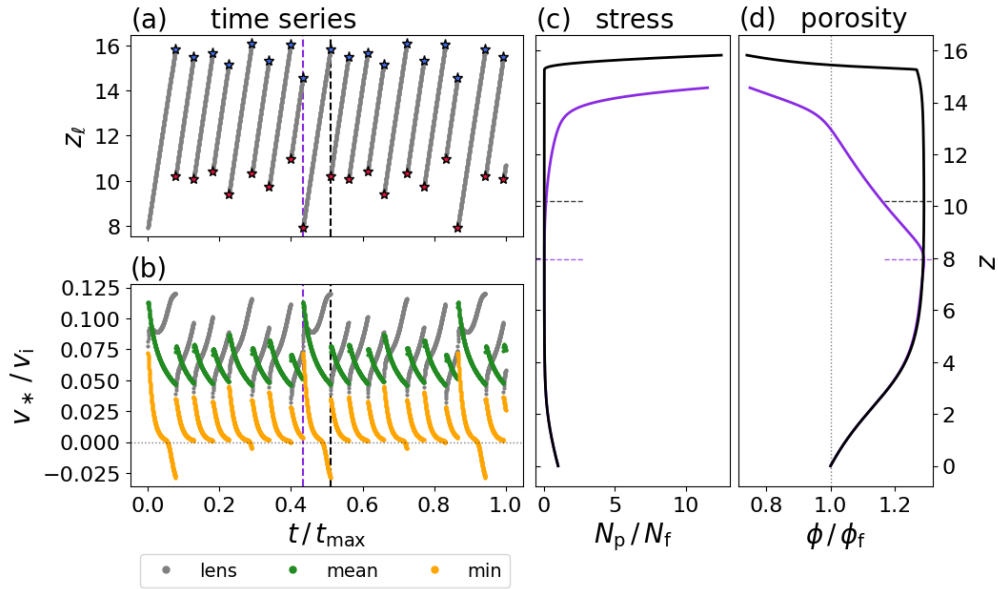


Figure 6. Evolution of the (a) ice lens position and (b) heave rate for the plastic compaction model ($\lambda = 0$) along with a comparison between vertical profiles from two different cycles (c,d). The pulling speed is $v_i = 0.038$ and the effective stress at the base of the fringe is set to $N_f = 2$, which corresponds to a porosity of $\phi_f = 0.325$. The maximum time is $t_{\max} = 3000$. (a) A multi-modal limit cycle in the fringe thickness arises for these parameter values, displaying eight distinct modes. (b) The heave rate below the ice lens displays an overall increasing trend, although there are cycles with non-monotonic behaviour. The mean heave rate within the fringe decreases over time as in the constant porosity model (figure 4) and the plastic compaction model at lower pulling speeds (figure 5). The minimum heave rate becomes negative for sustained periods of time, corresponding to a downward water flux due to compaction below the ice lens. (c) Stress profiles at the maximum fringe thickness for two successive cycles at the times noted by the dashed vertical lines in the time series. (d) Porosity profiles corresponding to the stress profiles in panel (c). Enhanced compaction at the larger fringe thickness (black line) leads to enhanced dilation below the compacting region.

For small values of the pulling speed (e.g., $v_i = 0.03$), periodic ice lens generation occurs in the perfectly plastic model in a similar manner to the constant porosity model (figure 5a). Time series of the maximum, minimum, and mean heave rate show that the heave rate decreases over time throughout the fringe as in the constant porosity model (figure 5b). Vertical profiles of the effective stress and porosity show that bulk dilation ($\phi > \phi_f$) occurs as the growing ice lens draws water into the fringe (figure 5c,d). New ice lenses nucleate where the porosity is maximized within the fringe. On the other hand, compaction ($\phi < \phi_f$) occurs directly below the ice lens due to the enhanced load (3.11) supported by particle contacts (figure 5d).

Compaction below the ice lens increases as the fringe thickens at larger pulling speeds. This enhanced compaction generates complex multi-modal cycles in the fringe thickness and heave rate. For example, a limit cycle with eight distinct modes is found at $v_i = 0.038$ (figure 6a). In this regime, the heave rate below the ice lens increases over time, corresponding to accelerated growth of the ice lens. Meanwhile, the heave rate often becomes negative within the fringe, which corresponds to a downward water flux (equation 2.9; figure 6b). Both of these behaviours arise because water is expelled out of the pore space due to the enhanced compaction below the ice lens (figure 6c,d). As in the constant porosity model, the mean heave rate decreases over time during each cycle because the mean permeability decreases as the fringe thickens. Thus, the overall rate of water supply to the ice lens still diminishes over time despite the different ways that this is accommodated within the fringe between the models.

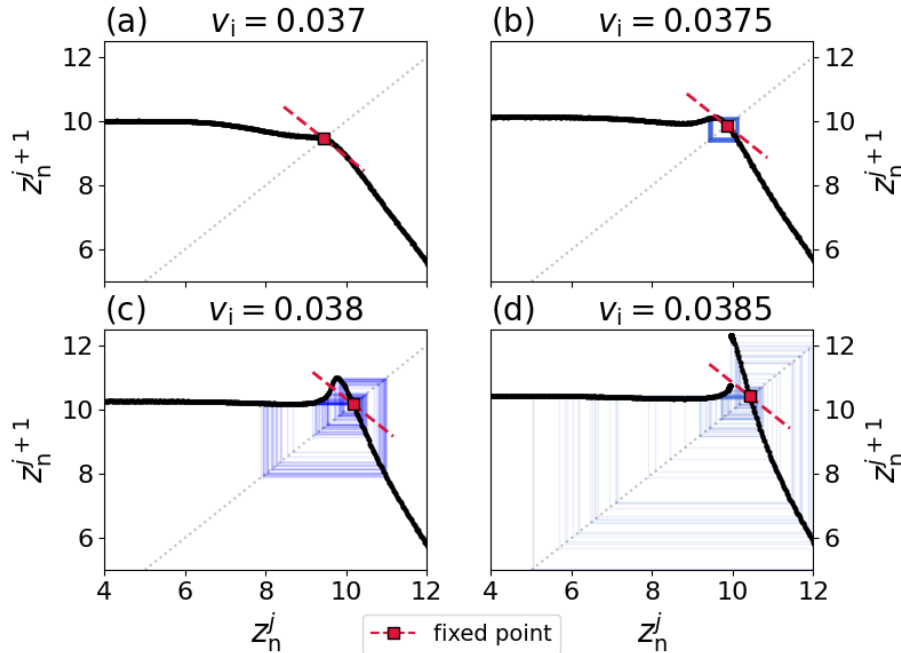


Figure 7. Recurrence relations between an incipient fringe thickness (z_n^j) and the next incipient fringe thickness (z_n^{j+1}) for a range of pulling speeds around the transition to complex oscillations. The fixed points of the mapping $z_n^{j+1} = f(z_n^j)$ are shown as red squares along with a slope of magnitude unity (dashed line) that characterises the stability. Blue lines show cobweb diagrams produced by iterating the interpolated map f two hundred times. (a) The fixed point is stable when $v_i = 0.037$, corresponding to a single-mode limit cycle. (b) The fixed point becomes unstable and a bimodal limit cycle arises near $v_i = 0.0375$. The fixed point remains unstable at higher pulling speeds. (c) The value $v_i = 0.038$ corresponds to the 8-mode limit cycle shown in figure 6. (d) Around $v_i = 0.0385$, the mapping f exhibits a discontinuity at $z_n^j \approx 10$ and chaotic behaviour arises.

The downward water flux causes porosity enhancement and weakening of the fringe in a spatially distributed zone below the compacting region (figure 6c,d). This weakening causes ice lenses to nucleate closer to the active ice lens. Thicker incipient fringes are inherently weaker and will not grow as large as the maximum thickness from a preceding cycle. Conversely, a thinner incipient fringe can grow to a maximum thickness that is larger than the preceding cycle before the downward water flux from enhanced compaction causes nucleation. These feedbacks give rise to the alternating behaviour in the multi-modal limit cycles (figure 6a).

To characterise the transition to multi-modal oscillations, we examine the recurrence relation between an incipient fringe thickness z_n^j and the next incipient fringe thickness z_n^{j+1} (figure 7). We approximate the mapping $z_n^{j+1} = f(z_n^j)$ by running the model for a range of initial conditions (z_n^j) until a new ice lens nucleates (z_n^{j+1}) and interpolating the results. When $v_i = 0.037$, there is a stable fixed point that corresponds to a single-mode limit cycle. The fixed point becomes unstable at higher values of v_i , resulting in multi-modal oscillations and increasing disorder (figure 7b-d). The recurrence relations show that the loss of stability is related to nucleation closer to the active ice lens (i.e., z_n^{j+1} increases), which is caused by the downward water flux from enhanced compaction below the ice lens at faster pulling speeds. Chaotic oscillations arise around $v_i = 0.0385$ (figure 7d).

The effective stress at the base of the fringe was $N_f = 2$ in all of the preceding examples (figures 4-8). To explore how the dynamics depend on this boundary condition, we construct bifurcation diagrams of the jumps in fringe thickness $z_m - z_n$ (ice lens spacing) relative to the pulling speed

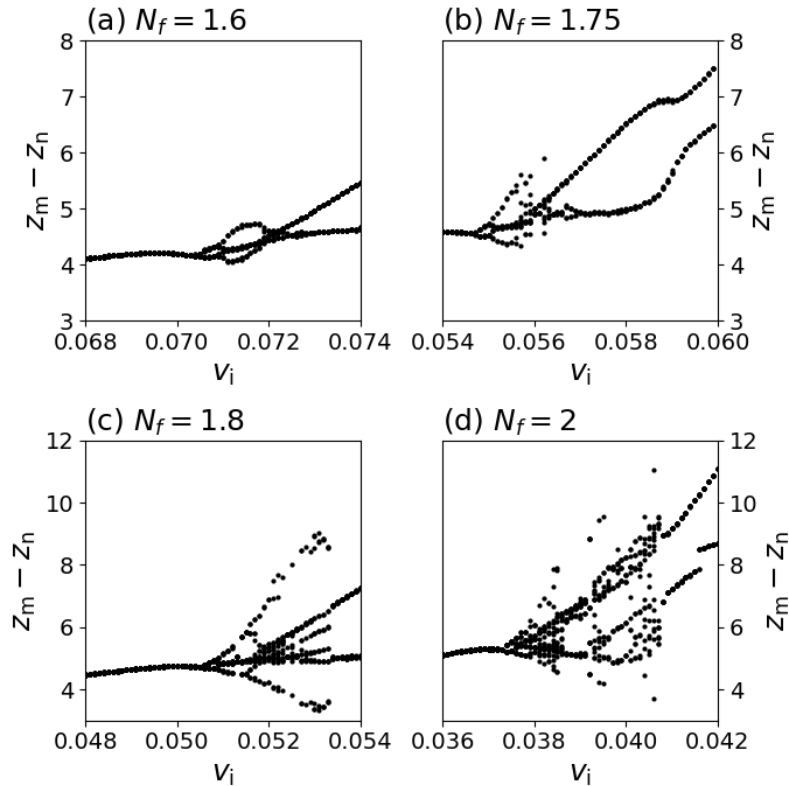


Figure 8. Frozen fringe thickness jumps $z_m - z_n$ (ice lens spacing) for different values of the effective stress boundary condition N_f . Disorder increases as the effective stress at the base of the fringe becomes larger. For each value of the effective stress boundary condition, unstable fringe growth (no periodic lenses) eventually occurs at higher values of the pulling speed v_i beyond what is shown in each panel. The value of the pulling speed v_i where multi-modal oscillations begin is sensitive to the effective stress at the base of the fringe N_f .

v_i for various values of N_f (figure 8). At smaller values of the effective stress condition ($N_f \lesssim 1.6$), multi-modal oscillations occur while the branches of the bifurcation diagram remain continuous (figure 8a). At higher values of the effective stress condition ($N_f \gtrsim 1.7$), the bifurcation diagrams become increasingly disordered (figure 8b-8d). A region of period doubling always precedes the more complex behaviour, which is a common route to chaos for discrete maps [59].

Disorder increases when the effective stress at the base increases because the frozen fringe must grow to a larger thickness before unloading can occur. In other words, the effects of enhanced compaction become more pronounced at larger N_f (figure 8). Likewise, the transition to multi-modal oscillations occurs at faster pulling speeds v_i for lower values of the effective stress condition N_f because the fringe must become sufficiently thick before the enhanced compaction influences the cycles. At pulling speeds beyond what is shown in figure 8, the water expelled from the pore space is distributed over an increasingly wider zone and the fringe growth effectively outpaces the weakening effective stress ($N \rightarrow 0$). Therefore, the fringe growth becomes unstable and no ice lenses nucleate in the limit of large v_i . This behaviour contrasts with the constant porosity model where periodic behaviour persists at large v_i because the heave rate and effective stress are independent of the pulling speed (section 3(c)).

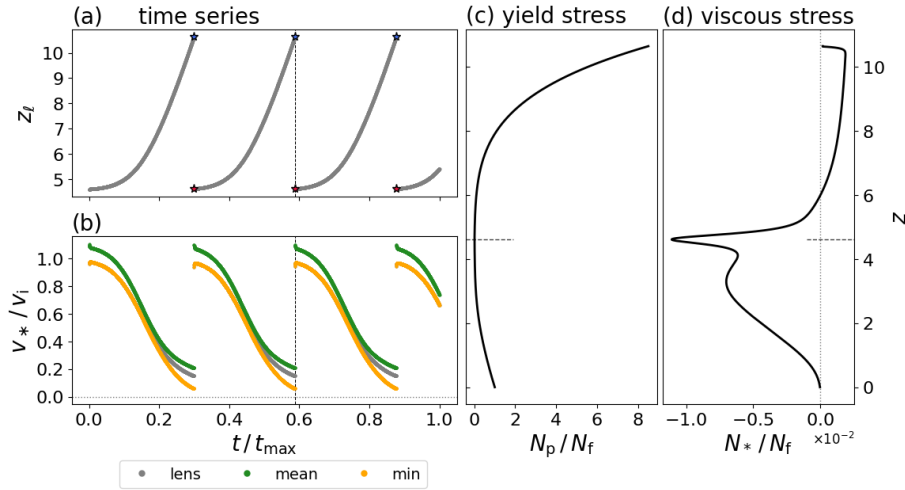


Figure 9. Evolution of the (a) ice lens position and (b) heave rate for the viscoplastic compaction model with the viscosity parameter $\lambda = 4$. The pulling speed is $v_i = 0.012$ and the effective stress at the base of the fringe is set to $N_f = 2$. The maximum time is $t_{max} = 4000$ and there is no tensile stress associated with cracking ($N_c = 0$). (a) Ice lenses are periodically generated for these values of the pulling speed and effective stress. (b) The heave rate decreases over time throughout the fringe for these parameters. (c) Plastic yield stress (N_p) profile at the maximum fringe thickness at the time noted by the dashed vertical line in the time series. (d) Viscous stress (N_*) profile at the maximum fringe thickness. Viscous decompaction ($N_* < 0$) drives ice lens nucleation at the position denoted by the horizontal dashed lines.

(c) Viscoplastic model

We now explore the effects of viscosity in the compaction law by setting $\lambda > 0$ in the full model (3.6)-(3.7). In this case, the compaction stress N_* (2.42) depends on the divergence of the solid velocity as in previous poroviscous mixture models [40]. We first consider the case where there is no tensile stress associated with cracking ($N_c = 0$) so that unloading ($N \rightarrow 0$) occurs solely through viscous decompaction. The width of the decompacting zone is sensitive to λ (2.43) because it primarily depends on the viscous compaction length scale δ (2.44). We set $\lambda = 4$, which corresponds to a viscous compaction length scale δ that is four times greater than the length scale set by infiltration [z]. For the parameters chosen herein, this corresponds to a bulk viscosity of $\zeta = 10^{13}$ Pa s (table 1), which is in the range of values for glacial ice [51,60].

Viscous decompaction provides the tensile stress necessary for unloading ($N \rightarrow 0$) to occur when $\lambda = 4$ (figure 9). At small values of the pulling speed (e.g., $v_i = 0.012$), repeating single-mode cycles occur in a similar manner to the constant porosity model. Likewise, the heave rate decreases over time throughout the fringe (figure 9a,b). Decompaction occurs in a localised zone within the fringe where the next ice lens nucleates (figure 9d). The plastic yield stress (N_p) is two orders of magnitude greater than the viscous stress (N_*) for these parameters (figure 9c).

At faster pulling speeds (e.g., $v_i = 0.02$), the effects of enhanced compaction below the ice lens begin to emerge (figure 10). In this regime, viscous decompaction occurs in a localised area below the compacting zone. A first nucleation event occurs directly below the compacting zone. The stress profile immediately after the first nucleation event is unstable ($N < 0$) and this immediately results in the nucleation of a second ice lens at a lower position within the fringe (figure 10c,d). This immediate second unloading event occurs because the region of enhanced compaction is cut off after nucleation and the instantaneous stress adjustment results in a transfer of viscous stresses to lower positions of the fringe where bulk dilation was building up during the cycle (figure 10c,d). The second nucleation event happens instantaneously in the model and corresponds to an ice lens of infinitesimal thickness. In this scenario, we envision that ice would

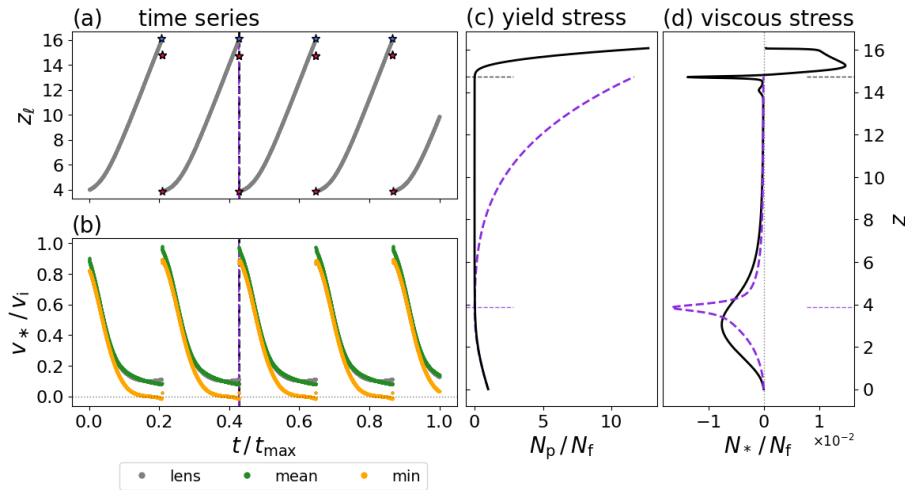


Figure 10. Evolution of the (a) ice lens position and (b) heave rate for the viscoplastic compaction model with the viscosity parameter $\lambda = 4$. The pulling speed is $v_i = 0.02$ and the effective stress at the base of the fringe is set to $N_f = 2$. The maximum time is $t_{\max} = 4000$ and there is no tensile stress associated with cracking ($N_c = 0$). (a) Pairs of ice lenses are periodically generated for these values of the pulling speed and effective stress. A first ice lens nucleates at a large fringe thickness and this is immediately followed by a second nucleation event at a smaller fringe thickness. (b) The heave rate is monotonically decreasing over time throughout the fringe for these parameters. (c) Plastic yield stress (N_p) profiles at the maximum fringe thickness at the time noted by the dashed vertical line in the time series. The solid line shows the stress profile for the maximum fringe thickness ($z_m \approx 16.1$) and the dashed line shows the stress profile for the incipient fringe thickness ($z_n \approx 14.7$). The incipient stress profile (dashed) has a region where $N < 0$, which immediately results in the nucleation of a new ice lens at $z_n \approx 3.9$. (d) Viscous stress (N_*) profiles corresponding to the profiles in (c). Viscous decompaction ($N_* < 0$) drives ice lens nucleation at the positions denoted by the horizontal dashed lines.

nucleate continuously for a small but finite length of time until an impermeable ice layer forms that cuts off water flow towards the active ice lens.

We have not found any other modes of oscillation in the viscoplastic problem when $\lambda > 1$. The lack of multi-modal or chaotic oscillations is due to the localised nature of decompaction below the ice lens. In particular, the removal of the compacting zone through nucleation of the first, unstable ice lens ultimately results in nucleation where bulk dilation was building up at lower positions within the fringe. Nucleation at higher positions within the fringe is effectively prevented, shutting down the instability in the recurrence relation that leads to complex oscillations in the perfectly plastic model (figure 7). This behaviour contrasts to the perfectly plastic model where the weakening occurs in a widely distributed zone below the ice lens, which allows for the feedbacks that lead to complex oscillations (figures 6c,d). In the viscous regime, the localised decompaction allows the oscillations to persist at large values of v_i as with the constant porosity model. This behaviour contrasts with the perfectly plastic regime where unstable fringe growth eventually occurs at fast ice velocities.

We examine how the oscillations vary over a range of λ to characterise the transition between viscous and perfectly plastic behaviour. The tensile stress associated with crack propagation is set to $N_c = 0.05$ to allow for unloading when the viscous effects are negligible. We calculate the jumps in frozen fringe thickness $z_m - z_n$ (ice lens spacing) with the parameters $v_i = 0.038$ and $N_f = 2$, which correspond to a multi-modal limit cycle in the perfectly plastic model (figure 6). The transition from complex oscillations in the plastic regime to paired nucleation events in the viscous regime occurs sharply at $\lambda \approx 0.31$ ($\zeta \approx 6 \times 10^{10}$ Pa s) for these parameters (figure 11). These results confirm that viscous decompaction effectively shuts down the instability that leads to the complex oscillations in the perfectly plastic model.

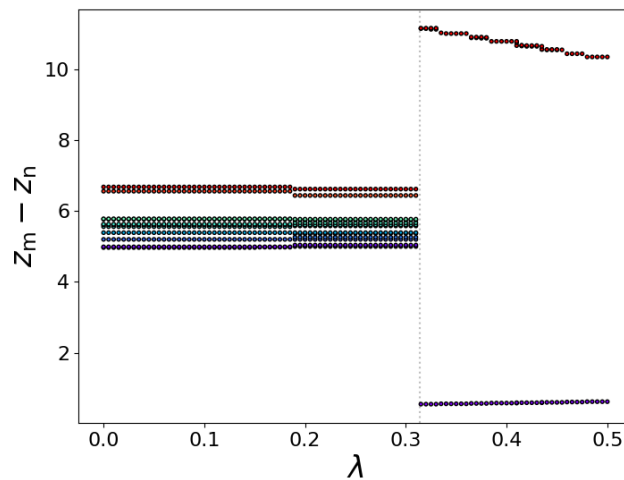


Figure 11. Frozen fringe thickness jumps $z_m - z_n$ (ice lens spacing) for different values of the viscosity parameter λ . Points are coloured to highlight the distinct modes at each value of λ . The pulling speed is set to $v_i = 0.038$ and the effective stress at the base of the fringe is set to $N_F = 2$, corresponding to the 8-mode limit cycle from the perfectly plastic model ($\lambda = 0$) shown in figure 6. A sharp change in behaviour occurs at $\lambda \approx 0.31$ due to the onset of viscous effects.

5. Discussion

The model developed herein shows that compaction below ice lenses influences the magnitude and duration of frost heave cycles. In the compaction models, we have found that the heave rate below the ice lens does not necessarily correspond to the mean heave rate within the fringe, which leads to substantial differences relative to the constant porosity model. At fast freezing rates, enhanced compaction below the ice lens causes a downward water flux and a zone of distributed weakening (dilation) in the perfectly plastic model. This weakening causes ice lenses to nucleate at higher positions within the fringe, which can lead to variations in ice lens spacing between successive cycles. When viscous effects are present, localised decompaction can cause the nucleation of an ice lens directly below the compacting zone, which effectively cuts off the compacting zone from the rest of the fringe and subsequently causes nucleation at lower positions within the fringe where bulk dilation occurs. These localised viscous effects can prevent the feedbacks that lead to multi-modal oscillations in the perfectly plastic model.

The nondimensional results in this study can be considered in the context of different temporal and spatial scales. In particular, the time scale $[t]$ (2.37) is primarily controlled by the permeability scale $[k]$, which can vary over many orders of magnitude [52,53]. With a permeability scale of $[k] = 6 \times 10^{-14} \text{ m}^2$ (table 1), heave rates are on the order of 10 cm/yr and new ice lenses form over a period of ~ 50 yr (e.g., figures 4-6). With a lower permeability of $[k] = 10^{-14} \text{ m}^2$, heave rates are on the order of 1 cm/yr and new ice lenses form over a period of ~ 300 yr. Sediment permeability is therefore expected to strongly influence the rates of ice accretion and sediment entrainment in subglacial environments, as well as the magnitude of frost heaving in cold regions.

The maximum frozen fringe thickness is influenced by the temperature gradient, which we set to 25 K/km here to coincide with conductive cooling beneath an ice sheet. In the examples herein, the maximum frozen fringe thickness reaches tens of metres. Frozen fringe thicknesses on the order of tens of metres could be associated with debris-rich ice beneath cold-based glaciers [16,61] or permafrost. While observations of subglacial permafrost are sparse [62], subaerial permafrost can be hundreds of metres thick [63,64]. Higher temperature gradients can arise in permafrost regions, especially the near-surface active layer that is strongly influenced by seasonal

1
2
3 temperature variations (e.g., >1 K/m) [65], as well as in laboratory experiments (e.g., >1 K/cm)
4 [35]. These higher temperature gradients result in stronger undercooling over smaller length
5 scales, which causes ice lens nucleation at smaller fringe thicknesses and shorter time scales than
6 those found in this study [36]. Likewise, the temperature gradient parameter c (table 1) likely
7 influences the ice velocities (or freezing rates) where the transition to complex oscillations occurs.

8 A similar transition to multi-modal oscillations and chaos was found at faster freezing rates
9 in theoretical and experimental studies of freezing colloidal suspensions [35,36]. While the
10 compacting region is located directly below the ice lens in our model, an evolving compaction
11 front was situated below the frozen fringe in the colloidal suspension model. Disorder increases
12 with the effective stress boundary condition at the base of the fringe in our study, whereas
13 disorder increased with the cohesive strength of the particle matrix in the colloidal suspensions
14 model [36]. A larger effective stress at the base of the fringe and a higher cohesive strength
15 of the particle matrix both require a larger fringe thickness to develop before lens nucleation
16 occurs, which could explain the common trends of increasing disorder between these studies.
17 Development of a simplified model that accounts for dilation and compaction within the fringe
18 in a similar fashion as the colloidal suspension model [36] could help to further characterise
19 the transitions and trends found herein. Despite the differences between the models and the
20 mechanisms that lead to the complex oscillations, both our perfectly plastic model and the
21 colloidal suspension model [36] show that compaction can strongly influence the fundamental
22 characteristics of frost heave cycles.

23 We explored two different mechanisms for lens initiation that were associated with the
24 propagation of ice-filled cracks and, alternatively, cleaving of the particle matrix by viscous
25 intrusion. Propagation of ice-filled cracks within fine-grained sediment has previously been
26 proposed as a mechanism for nucleating ice lenses even when a frozen fringe is absent [48,49].
27 While numerous laboratory experiments support the crack propagation mechanism [34,66–71],
28 some experiments show ice lenses separated by undisturbed sediment with no clear evidence
29 of cracking [12,32]. Further exploration of comprehensive dynamic cracking models would be
30 valuable for elucidating the patterns observed in laboratory experiments and the conditions
31 under which cracking is a viable mechanism for ice lens nucleation [72].

32 We have found that an alternative mechanism for lens nucleation by viscous decompaction
33 can be modelled by including a bulk viscosity in the compaction law that is the same order of
34 magnitude as the viscosity of glacial ice. However, the viscous decompaction mechanism can lead
35 to the absence of the complex dynamics that have been found in some laboratory experiments
36 [35,36]. Ultimately, these different nucleation mechanisms and compaction laws will need to be
37 evaluated experimentally in the laboratory in relation to the basic characteristics of frost heave
38 cycles as well as the stability of ice lens and frozen fringe growth under different thermal regimes.

39 The model developed herein can be generalised to higher spatial dimensions by following the
40 mixture theory approach [40]. The primary computational challenge in extending the model to
41 higher dimensions is that the water flux divergence (2.8) cannot be integrated, which requires the
42 solution of an additional coupled equation. This generalisation would be useful for modelling
43 horizontal variations in effective stress or temperature that could be related to differential frost
44 heave and patterned ground formation in the Arctic [49,73,74], as well as the polygonal cracking
45 structures that have been observed in laboratory experiments [33,68,69]. Moreover, we expect that
46 the development of high-porosity shear bands that were found in the ring shear experiment could
47 be analysed with a two-dimensional model in a similar fashion to previous studies on partially
48 molten rocks (figure 1c) [27–30].

49 We assumed that the ice was rigid in our analysis for comparison with previous models
50 and quantified the validity of this approximation in the case of a purely vertical force balance
51 (Appendix). However, the validity of this assumption is unclear under shearing conditions
52 when the ice skeleton could presumably be deformed. For example, deforming debris-rich ice
53 is especially common in subglacial environments [16,20]. The model developed herein can be
54 extended to include the effects of deforming ice by generalising the ice momentum balance (2.14)

to include deviatoric stresses via flow laws that are appropriate for glacial ice [50,51,60]. This generalisation would be valuable for modelling the effects of ice deformation on fringe evolution and the mechanics of sliding at glacier beds [18,22,24,26].

6. Conclusions

Here, we introduced a mathematical model for the mechanics of partially frozen sediment that accounts for compaction and dilation during frost heave. The model follows a similar structure to mixture theories that were previously developed for partially molten rocks. The primary differences in our model are that the compaction law incorporates plastic yield stresses from soil consolidation while the interfacial forces allow for rigid ice skeletons and premelting effects. We explored the fundamental characteristics of frost heave cycles generated by pulling frozen fringe through a fixed temperature gradient for perfectly plastic and viscoplastic compaction laws. In the perfectly plastic model, the ice lens spacing can vary between cycles at faster pulling speeds. A transition to complex oscillations and chaos is associated with the formation of a distributed zone of dilation, or weakening, from the downward water flux due to enhanced compaction directly beneath the ice lens. Viscous effects prevent these feedbacks from occurring by introducing localised zones of decompaction. These comparisons show that the physics of compaction within the frozen fringe exert strong control on the magnitude and duration of frost heave cycles. In addition to generalising the model to higher spatial dimensions and deforming ice, future work should focus on constraining ice lens nucleation conditions and compaction laws for frozen fringe to further elucidate the mechanics of ice segregation in freezing soils.

Acknowledgements. We thank the editor and referees for reviewing the manuscript. This research was funded by the Office of Polar Programs, U.S. National Science Foundation (2012958, 2013987).

Appendix. Rigid ice approximation

To quantify the validity of the rigid ice assumption (i.e., constant v_i), we consider the effects of viscous ice deformation where the normal stress is given by $\sigma_i = p_i - 2\eta \frac{\partial v_i}{\partial z}$ for a constant ice viscosity η . Under this assumption, equation (2.14) becomes

$$\Phi \left(-2\eta \frac{\partial^2 v_i}{\partial z^2} + \frac{\partial p_i}{\partial z} + \rho_i g \right) = 2\eta \frac{\partial v_i}{\partial z} \frac{\partial \Phi}{\partial z}, \quad (6.1)$$

where we have defined the ice volume fraction $\Phi(z) = \phi(z)S(z)$. We decompose the pressure gradient via $\frac{\partial p_i}{\partial z} = -\rho_i g + \frac{\partial \tilde{p}}{\partial z}$ where \tilde{p} is the perturbation from the cryostatic pressure. Without renaming the variables, equation (6.1) scales to

$$-\frac{\partial^2 v_i}{\partial z^2} = \frac{1}{\Phi} \frac{\partial v_i}{\partial z} \frac{\partial \Phi}{\partial z} - \nu \frac{\partial \tilde{p}}{\partial z}, \quad (6.2)$$

where $\nu = [p][z]/(2\eta[v])$ with $[p]$ being the pressure perturbation scale, which we leave arbitrary for now. Setting $v_i(z_\ell) = V$ for a given ice velocity at the lens V , the solution to (6.2) is

$$v_i(z) = V + \nu \int_z^{z_\ell} \frac{1}{\Phi(s)} \left[\int_0^s \Phi(s') \frac{\partial \tilde{p}}{\partial s'} ds' \right] ds. \quad (6.3)$$

Integrating the inner integral in (6.3) by parts and using $\Phi(0) = 0$ results in

$$v_i(z) = V + \nu \int_z^{z_\ell} \tilde{p}(s) - \frac{1}{\Phi(s)} \left[\int_0^s \tilde{p}(s') \frac{\partial \Phi}{\partial s'} ds' \right] ds. \quad (6.4)$$

We assume that the ice mass increases monotonically towards the lens ($\Phi'(z) > 0$) and thereby apply the mean value theorem to the inner integral in (6.4) to obtain

$$v_i(z) = V + \nu \int_z^{z_\ell} \tilde{p}(s) - \tilde{p}(\xi(s)) ds, \quad (6.5)$$

where $\xi(s) \in (0, s)$ for each value of s . Using the triangle inequality, we estimate from (6.5) that

$$\max |v_i - V| \leq 2\nu z_\ell \max |\tilde{p}|. \quad (6.6)$$

The inequality (6.6) quantifies the maximum deviation of the ice velocity from a constant value V (i.e. the rigid ice solution) as a function of the parameter $\nu = [p][z]/(2\eta[v])$, the fringe thickness z_ℓ , and the magnitude of the pressure perturbation \tilde{p} . For example, with a pressure perturbation scale of $[p] = 10$ kPa (i.e., a fraction of $[N] = 68$ kPa) and ice viscosity of $\eta = 5 \times 10^{14}$ Pa s, the parameter $\nu \approx 9 \times 10^{-5}$ for the length scale $[z] = 4.62$ m and velocity scale $[v] = 15.5$ m/yr (table 1), which suggests that the rigid ice approximation is appropriate for these parameters.

References

1. O'Neill K, Miller RD. 1985 Exploration of a rigid ice model of frost heave. *Water Resources Research* **21**, 281–296.
2. Fowler A. 1989 Secondary frost heave in freezing soils. *SIAM Journal on Applied Mathematics* **49**, 991–1008.
3. Fowler AC, Krantz WB. 1994 A generalized secondary frost heave model. *SIAM Journal on Applied Mathematics* **54**, 1650–1675.
4. Rempel AW, Wettlaufer J, Worster MG. 2004 Premelting dynamics in a continuum model of frost heave. *Journal of fluid mechanics* **498**, 227–244. ([10.1017/S0022112003006761](https://doi.org/10.1017/S0022112003006761))
5. Rempel A. 2007 Formation of ice lenses and frost heave. *Journal of Geophysical Research: Earth Surface* **112**. ([10.1029/2006JF000525](https://doi.org/10.1029/2006JF000525))
6. Meyer CR, Schoof C, Rempel AW. 2023 A thermomechanical model for frost heave and subglacial frozen fringe. *Journal of Fluid Mechanics* **964**, A42. ([10.1017/jfm.2023.366](https://doi.org/10.1017/jfm.2023.366))
7. Cahn J, Dash J, Fu H. 1992 Theory of ice premelting in monosized powders. *Journal of crystal growth* **123**, 101–108.
8. Dash J, Rempel A, Wettlaufer J. 2006 The physics of premelted ice and its geophysical consequences. *Reviews of modern physics* **78**, 695.
9. Wettlaufer JS, Worster MG. 2006 Premelting dynamics. *Annu. Rev. Fluid Mech.* **38**, 427–452.
10. Rempel A, Wettlaufer J, Worster M. 2001 Interfacial premelting and the thermomolecular force: thermodynamic buoyancy. *Physical review letters* **87**, 088501.
11. Taber S. 1929 Frost heaving. *The Journal of Geology* **37**, 428–461.
12. Taber S. 1930 The mechanics of frost heaving. *The Journal of Geology* **38**, 303–317.
13. Mackay JR. 1971 The origin of massive icy beds in permafrost, western Arctic coast, Canada. *Canadian Journal of Earth Sciences* **8**, 397–422.
14. Waller RI, Murton JB, Knight PG. 2009 Basal glacier ice and massive ground ice: different scientists, same science?. *Geological Society, London, Special Publications* **320**, 57–69.
15. Kanevskiy M, Shur Y, Jorgenson M, Ping CL, Michaelson G, Fortier D, Stephani E, Dillon M, Tumskoy V. 2013 Ground ice in the upper permafrost of the Beaufort Sea coast of Alaska. *Cold Regions Science and Technology* **85**, 56–70.
16. Knight PG. 1997 The basal ice layer of glaciers and ice sheets. *Quaternary Science Reviews* **16**, 975–993.
17. Christoffersen P, Tulaczyk S, Carsey FD, Behar AE. 2006 A quantitative framework for interpretation of basal ice facies formed by ice accretion over subglacial sediment. *Journal of Geophysical Research: Earth Surface* **111**.
18. Rempel AW. 2008 A theory for ice-till interactions and sediment entrainment beneath glaciers. *Journal of Geophysical Research: Earth Surface* **113**. (<https://doi.org/10.1029/2007JF000870>)
19. Meyer CR, Robel AA, Rempel AW. 2019 Frozen fringe explains sediment freeze-on during Heinrich events. *Earth and Planetary Science Letters* **524**, 115725.
20. Moore PL. 2014 Deformation of debris-ice mixtures. *Reviews of Geophysics* **52**, 435–467.
21. Meyer CR, Downey AS, Rempel AW. 2018 Freeze-on limits bed strength beneath sliding glaciers. *Nature communications* **9**, 3242.
22. Lipovsky BP, Meyer CR, Zoet LK, McCarthy C, Hansen DD, Rempel AW, Gimbert F. 2019 Glacier sliding, seismicity and sediment entrainment. *Annals of Glaciology* **60**, 182–192.
23. Thompson A, Iverson N, Zoet L. 2020 Controls on subglacial rock friction: Experiments with debris in temperate ice. *Journal of Geophysical Research: Earth Surface* **125**, e2020JF005718.
24. Rempel AW, Hansen DD, Zoet LK, Meyer CR. 2023 Diffuse debris entrainment in glacier, lab and model environments. *Annals of Glaciology* pp. 1–13.

25. Zoet L, Sobol P, Lord N, Hansen D. 2023 A ring shear device to simulate cryosphere processes. *Review of Scientific Instruments* **94**.
26. Hansen DD, Warburton KLP, Zoet LK, Meyer CR, Rempel AW, Stubblefield AG. 2024 Presence of Frozen Fringe Impacts Soft-Bedded Slip Relationship. *Geophysical Research Letters* **51**, e2023GL107681. e2023GL107681 2023GL107681 (<https://doi.org/10.1029/2023GL107681>)
27. Spiegelman M. 2003 Linear analysis of melt band formation by simple shear. *Geochemistry, Geophysics, Geosystems* **4**.
28. Katz RF, Spiegelman M, Holtzman B. 2006 The dynamics of melt and shear localization in partially molten aggregates. *Nature* **442**, 676–679.
29. Katz RF, Takei Y. 2013 Consequences of viscous anisotropy in a deforming, two-phase aggregate. Part 2. Numerical solutions of the full equations. *Journal of Fluid Mechanics* **734**, 456–485.
30. Takei Y, Katz RF. 2013 Consequences of viscous anisotropy in a deforming, two-phase aggregate. Part 1. Governing equations and linearized analysis. *Journal of Fluid Mechanics* **734**, 424–455.
31. Mutou Y, Watanabe K, Ishizaki T, Mizoguchi M. 1998 Microscopic observation of ice lensing and frost heave in glass beads. In *Proceedings of the 7th International Conference on Permafrost* pp. 23–27. Centre d'études nordiques, Univ. Laval Quebec, QC, Canada.
32. Watanabe K, Mizoguchi M. 2000 Ice configuration near a growing ice lens in a freezing porous medium consisting of micro glass particles. *Journal of Crystal Growth* **213**, 135–140. ([https://doi.org/10.1016/S0022-0248\(00\)00353-5](https://doi.org/10.1016/S0022-0248(00)00353-5))
33. Peppin S, Elliott J, Worster MG. 2006 Solidification of colloidal suspensions. *Journal of Fluid Mechanics* **554**, 147–166.
34. Peppin SS, Worster MG, Wettlaufer J. 2007 Morphological instability in freezing colloidal suspensions. *Proceedings of the royal society a: mathematical, physical and engineering sciences* **463**, 723–733.
35. Anderson AM, Worster MG. 2012 Periodic ice banding in freezing colloidal dispersions. *Langmuir* **28**, 16512–16523.
36. Anderson AM, Worster MG. 2014 Freezing colloidal suspensions: periodic ice lenses and compaction. *Journal of Fluid Mechanics* **758**, 786–808. ([10.1017/jfm.2014.500](https://doi.org/10.1017/jfm.2014.500))
37. Audet D, Fowler A. 1992 A mathematical model for compaction in sedimentary basins. *Geophysical Journal International* **110**, 577–590.
38. Tulaczyk S, Kamb WB, Engelhardt HF. 2000 Basal mechanics of ice stream B, West Antarctica: 1. Till mechanics. *Journal of Geophysical Research: Solid Earth* **105**, 463–481.
39. Tulaczyk S, Kamb B, Engelhardt HF. 2001 Estimates of effective stress beneath a modern West Antarctic ice stream from till preconsolidation and void ratio. *Boreas* **30**, 101–114.
40. McKenzie D. 1984 The generation and compaction of partially molten rock. *Journal of petrology* **25**, 713–765. ([10.1093/petrology/25.3.713](https://doi.org/10.1093/petrology/25.3.713))
41. Spiegelman M, Cox KG, McKenzie DP, White RS. 1993 Physics of melt extraction: theory, implications and applications. *Philosophical Transactions of the Royal Society of London. Series A: Physical and Engineering Sciences* **342**, 23–41. ([10.1098/rsta.1993.0002](https://doi.org/10.1098/rsta.1993.0002))
42. Schoof C, Hewitt IJ. 2016 A model for polythermal ice incorporating gravity-driven moisture transport. *Journal of Fluid Mechanics* **797**, 504–535. ([10.1017/jfm.2016.251](https://doi.org/10.1017/jfm.2016.251))
43. Hewitt DR, Paterson DT, Balmforth NJ, Martinez DM. 2016 Dewatering of fibre suspensions by pressure filtration. *Physics of Fluids* **28**, 063304. ([10.1063/1.4952582](https://doi.org/10.1063/1.4952582))
44. Kvick M, Martinez DM, Hewitt DR, Balmforth NJ. 2017 Imbibition with swelling: Capillary rise in thin deformable porous media. *Physical Review Fluids* **2**, 074001.
45. Bercovici D, Ricard Y, Schubert G. 2001 A two-phase model for compaction and damage: 1. General Theory. *Journal of Geophysical Research: Solid Earth* **106**, 8887–8906. (<https://doi.org/10.1029/2000JB900430>)
46. Worster MG. 2000 Solidification of fluids. In Worster MG, Batchelor G, Moffatt H, editors, *Perspectives in Fluid Dynamics*, pp. 393–444. Cambridge University Press Cambridge.
47. Style RW, Gerber D, Rempel AW, Dufresne ER. 2023 The generalized Clapeyron equation and its application to confined ice growth. *Journal of Glaciology* **69**, 1091–1096. ([10.1017/jog.2023.28](https://doi.org/10.1017/jog.2023.28))
48. Style RW, Peppin SS, Cocks AC, Wettlaufer JS. 2011 Ice-lens formation and geometrical supercooling in soils and other colloidal materials. *Physical Review E* **84**, 041402.
49. Peppin SS, Style RW. 2013 The physics of frost heave and ice-lens growth. *Vadose Zone Journal* **12**, 1–12.

- 1
2
3 50. Glen JW. 1955 The creep of polycrystalline ice. *Proceedings of the Royal Society of London. Series A. Mathematical and Physical Sciences* **228**, 519–538.
- 4 51. Cuffey KM, Paterson WSB. 2010 *The physics of glaciers*. Academic Press.
- 5 52. Fischer UH, Iverson NR, Hanson B, Hooke RL, Jansson P. 1998 Estimation of hydraulic
6 properties of subglacial till from ploughmeter measurements. *Journal of Glaciology* **44**, 517–522.
- 7 53. Warburton K, Hewitt D, Neufeld J. 2023 Shear dilation of subglacial till results in time-
8 dependent sliding laws. *Proceedings of the Royal Society A* **479**, 20220536.
- 9 54. Zoet LK, Iverson NR. 2020 A slip law for glaciers on deformable beds. *Science* **368**, 76–78.
- 10 55. Zoet LK, Iverson NR, Andrews L, Helanow C. 2022 Transient evolution of basal drag during
11 glacier slip. *Journal of Glaciology* **68**, 741–750.
- 12 56. Alnæs MS, Logg A, Ølgaard KB, Rognes ME, Wells GN. 2014 Unified Form Language: A
13 Domain-Specific Language for Weak Formulations of Partial Differential Equations. *ACM*
14 *Trans. Math. Softw.* **40**. ([10.1145/2566630](https://doi.org/10.1145/2566630))
- 15 57. Scroggs MW, Dokken JS, Richardson CN, Wells GN. 2022a Construction of Arbitrary Order
16 Finite Element Degree-of-Freedom Maps on Polygonal and Polyhedral Cell Meshes. *ACM*
17 *Trans. Math. Softw.* **48**. ([10.1145/3524456](https://doi.org/10.1145/3524456))
- 18 58. Scroggs MW, Baratta IA, Richardson CN, Wells GN. 2022b Basix: a runtime finite element
19 basis evaluation library. *Journal of Open Source Software* **7**, 3982. ([10.21105/joss.03982](https://doi.org/10.21105/joss.03982))
- 20 59. Strogatz SH. 2018 *Nonlinear dynamics and chaos: with applications to physics, biology, chemistry,*
21 *and engineering*. CRC press. ([10.1201/9780429492563](https://doi.org/10.1201/9780429492563))
- 22 60. Greve R, Blatter H. 2009 *Dynamics of ice sheets and glaciers*. Springer Science & Business Media.
- 23 61. Hubbard B, Sharp M. 1989 Basal ice formation and deformation: a review. *Progress in Physical*
24 *Geography* **13**, 529–558.
- 25 62. Alexander A, Obu J, Schuler TV, Käab A, Christiansen HH. 2020 Subglacial permafrost
26 dynamics and erosion inside subglacial channels driven by surface events in Svalbard. *The*
27 *Cryosphere* **14**, 4217–4231. ([10.5194/tc-14-4217-2020](https://doi.org/10.5194/tc-14-4217-2020))
- 28 63. Osterkamp T, Payne M. 1981 Estimates of permafrost thickness from well logs in northern
29 Alaska. *Cold Regions Science and Technology* **5**, 13–27.
- 30 64. Wu Q, Zhang T, Liu Y. 2010 Permafrost temperatures and thickness on the Qinghai-Tibet
31 Plateau. *Global and Planetary Change* **72**, 32–38.
- 32 65. Smith SL, O'Neill HB, Isaksen K, Noetzli J, Romanovsky VE. 2022 The changing thermal state
33 of permafrost. *Nature Reviews Earth & Environment* **3**, 10–23.
- 34 66. Akagawa S. 1988 Experimental study of frozen fringe characteristics. *Cold Regions Science and*
35 *Technology* **15**, 209–223.
- 36 67. Arenson LU, Segó DC, Take WA. 2007 Measurement of ice lens growth and soil consolidation
37 during frost penetration using particle image velocimetry (PIV). In *60th Canadian Geotechnical*
38 *Conference, Ottawa, ON* pp. 2046–2053.
- 39 68. Arenson LU, Azmatch TF, Segó DC, Biggar K. 2008 A new hypothesis on ice lens formation in
40 frost-susceptible soils. In *Proceedings of the ninth international conference on permafrost, Fairbanks,*
41 *Alaska* vol. 1 pp. 59–64.
- 42 69. Azmatch TF, Segó DC, Arenson LU, Biggar KW. 2012 New ice lens initiation condition for
43 frost heave in fine-grained soils. *Cold Regions Science and Technology* **82**, 8–13.
- 44 70. Wang Y, Wang D, Ma W, Wen Z, Chen S, Xu X. 2018 Laboratory observation and analysis of
45 frost heave progression in clay from the Qinghai-Tibet Plateau. *Applied Thermal Engineering*
46 **131**, 381–389.
- 47 71. Zheng H, Sasaki Y, Kanie S. 2020 Image processing method for observing ice lenses produced
48 by the frost heave process. *Cold Regions Science and Technology* **171**, 102977.
- 49 72. Suh HS, Sun W. 2022 Multi-phase-field microporomechanics model for simulating ice-lens
50 growth in frozen soil. *International Journal for Numerical and Analytical Methods in Geomechanics*
51 **46**, 2307–2336.
- 52 73. Peterson RA, Krantz WB. 2003 A mechanism for differential frost heave and its implications
53 for patterned-ground formation. *Journal of Glaciology* **49**, 69–80.
- 54 74. Peterson R, Krantz W. 2008 Differential frost heave model for patterned ground formation:
55 Corroboration with observations along a North American arctic transect. *Journal of Geophysical*
56 *Research: Biogeosciences* **113**.